Segmentation of Breast Region from MR Images using Multi-State Cellular Neural Networks

Dogan D.Demirgüneş[1], Gökhan Ertaş[2], Turan Ilıca[3], Osman Eroğul[1], and Ziya Telatar[4]

[1]Gülhane Military Medical Academy, Biomedical Engineering Center, Ankara, Turkey
{ddemirgunes, oerogul}@gata.edu.tr
[2]Yeditepe University, Faculty of Engineering and Architecture, Biomedical Engineering Department, Istanbul, Turkey
[3]Gülhane Military Medical Academy, Radiology Department, Ankara, Turkey
[4]Ankara University, Faculty of Engineering, Electronics Engineering Department, Ankara, Turkey

Abstract

Computer assisted evaluation of magnetic resonance (MR) images for breast density assessment or lesion localization requires accurate separation of breast tissues from other tissues and regions of the body, such as the chest muscle, lungs, heart and ribs. In this study, we introduce a semi-automated algorithm that segments breast region from non fat-suppressed T2-weighted axial breast MR images. The algorithm employs three specially designed multi-state cellular neural networks (CNNs) connected in cascade. Analysis of 106 high-resolution images from 23 women acquired using a 3T MR scanner shows that the algorithm is exceptionally effective with high precision, high true-positive volume fraction, and low false-positive volume fraction with an overall performance of 99.1±2.0%, 99.4±1.4%, and 0.1±0.2%, respectively. The use of multi-state CNN reduces the false segmentations on the images due to noise, intensity inhomogeneity and partial volume artifacts.

1. Introduction

For the diagnosis of breast cancer and the differential diagnosis of enhancing lesions, magnetic resonance imaging (MRI) is gaining increased acceptance resulting in the accumulation of high-spatial resolution cross-sectional morphology and enhancement information that reflects vascularity and permeability of breast tissues [1]. When compared to x-ray mammography, breast MRI provides superior detection and classification of invasive cancer and it is more sensitive for ductal carcinoma in situ in high risk women [2]. Moreover, breast MRI offers the potential for accurate measurement of fibroglandular tissue volume to assess breast density, which is a strong risk factor associated with the development of breast cancer [3]. To improve interpretation accuracy and reproducibility further, there is an apparent need for computer assistance to process the large volume of image data produced with high spatial and temporal resolution during an MR scan [4]. For breast density assessment or lesion localization, computer assisted evaluation of MR images requires accurate separation of breast tissues from other tissues and regions of the body, such as the chest muscle, lungs, heart and ribs. Breast region can be segmented as the middle section between breast-air and breast-chest wall boundaries. High contrast between these boundaries is obtained when non fat-suppressed images are used. On these images, the breast-air boundary is identified easily by searching for a sharp increase in the image intensity from the air side provided that the background noise is low. However, breast-chest wall boundary detection is a complicated problem due to partial volume and intensity inhomogeneity artifacts, especially in the presence of dense breast tissue connected to the chest wall muscles and liver tissue underneath the muscles.

Hayton et al. [5] used dynamic programming to detect breast-air boundary and iterative morphological erosion followed by dilation and graph search to find an approximate location of the chest wall. For certain patients, the algorithm generates satisfactory results but it requires a long process time and fails if the patient's chest is not flat. Koenig at al. [6] employed histogram quantiles for gray level thresholding and intensity gradients to detect breast tissue as boundaries. It requires the exact location of the nipples and is able to segment the chest-wall boundary very roughly. Lu et al. [7] developed a method based on mathematical morphology and region growing to locate the breast-air boundary and an active contour model to locate the breast-chest-wall boundary. The performance of the algorithm depends on appropriate selection of the field of view and makes several assumptions such as the locations of the axilla, midsternum, and nipples. It fails for those patients with large breasts where the left and right sides are compressed together. Nie et al [8] proposed an initial segmentation based on body landmarks followed by simple fuzzy c-mean clustering to determine air and lung tissue, B-spline fitting to locate the chest wall and dynamic searching to remove the breast skin edge. This algorithm requires appropriate selection of the field of view and intensive user interaction in each step. It fails when the locations of the spinous process of the thoracic spine or the lateral margin of the bilateral pectoralis muscles are undetectable from images.

Segmentation methods that do not require prior information concerning breast anatomy have been also studied. Arbach et al. [9] introduced a method based on dynamic programming that processes computed edge enhanced images. Twellmann et al. [10] reported a simple technique that consists of median filtering, gray-level-based histogram thresholding using Otsu's method [11], and morphological closing. Better results are obtained when Otsu's method is replaced with k-means clustering [12]. Yao et al. [13] used active contours to locate the air-breast boundary and dynamic searching to locate the chest wall. Ertas et al. [14] proposed a cellular neural network that performs gray-level thresholding, biggest region detection and morphological erosion followed by reconstruction.

All of the methods mentioned above are designed to work on certain images and are able to generate satisfactory results for given degrees of background noise, intensity inhomogeneity and partial volume artifacts. Background noise produces apparent

signal from regions containing air in the images. Intensity inhomogeneity artifacts show up as anatomically irrelevant intensity variations on the image mainly induced by the physical properties of the receiver surface coil. Partial volume artifacts lead to ambiguities in structural definitions on the data blurring intensities across boundaries where different tissues contribute to a single voxel. Since these effects are due to complex electromagnetic interactions between the imaged tissue and the acquisition system, they cannot be reduced by simple calibrations before scanning.

In this study, we introduce a semi-automated segmentation algorithm that uses non fat-suppressed T2-weighted axial images and minimizes the impact of the artifacts described above. The images are processed by three specially designed multi-state cellular neural networks connected in cascade. Statistical analysis results show that the algorithm requires minimal user interaction and exceptionally effective for segmenting the breast.

2. Materials and Methods

2.1. Imaging Protocol

Magnetic resonance imaging is conducted on a 3.0T MR imager (Achieva, Philips Medical Systems Netherlands). Patients are placed in a prone position during the scan to minimize motion artifacts. A dedicated 8-channel integrated SENSE receiver breast coil is used. The imaging sequence is a variant of 3D T2-weighted Turbo Spin Echo sequence (VISTA), (TR/TE 2000/251ms, flip angle 90°, slice thickness 1 mm, resolution $0,75 \times 0,75 \text{mm}^2$ in x- and y-directions).

2.2. Patient Population and Image Dataset

The dataset analyzed in this study consists of 106 axial bilateral breast MR images from 23 women (age: 21–69 years, mean age: 45.5 years) that covers 36 fatty, 42 fibroglandular or heterogeneously dense and 28 dense breast slices in a range of sizes. All 12-bit grayscale images are transferred in a DICOM format from the imaging device to a personnel computer for analysis with the approval of Ethics Committee of Gülhane Medical Military Academy (Ankara, Turkey).

2.3. Breast Region Segmentation using Multi-State Cellular Neural Networks

Cellular Neural Networks (CNNs) provide an alternative way to perform morphological operations [15]. Since CNNs can be implemented in hardware using special CNN chips, images can be processed in real-time; for example, a basic morphological operation can be completed within 1μs, independent of the image size and the structuring elements [16].

CNNs are locally interconnected cells arranged into arrays (regularly spaced positions). Consider a 2D $M \times N$ image and a cell located at position (i, j), $i=1,2,\dots,M$, $j=1,2,\dots,N$. The r-neighborhood of the cell located at position (i, j) is defined by

$$N_{i,j}(r) = \left\{ C_{m,n} \mid \max(|m-i|,|n-j|) \le r; \ 1 \le m \le M, \ 1 \le n \le N \right\} \quad (1)$$

where r is a positive integer. The output $y_t(i, j)$ and the state $x_t(i, j)$ at this location at iteration $t \ge 1$ can be described by the following equations [17]:

$$y_t(i, j) = g\left(x_{t-1}(i, j)\right) \quad (2)$$

$$x_t(i, j) = \sum_{(m,n) \in N_{i,j}(r)} A_{m,n} \times y_t(i+m, j+n)$$
$$+ \sum_{(m,n) \in N_{i,j}(r)} B_{m,n} \times u(i+m, j+n) + b \quad (3)$$

where $g(.)$ is a monotonous decreasing function. $u(i, j)$ is the input, $A_{m,n}$ and $B_{m,n}$ are the entries at the m,n-th neighborhood of the feedback and control templates and b is a constant bias parameter. The input and the initial states are assumed to have a magnitudes less than or equal to 1.

CNNs can also be so designed that the state and therefore the feedback template and the output may be in multi-dimension with dedicated $g(.)$ functions. For instance, the state may be a doublet defined by

$$x_t^{(1)}(i, j) = l_t(i, j) \quad (4)$$

$$x_t^{(2)}(i, j) = s_t(i, j) \quad (5)$$

where $l_t(i, j)$ is the label, $s_t(i, j)$ is the strength. Then the feedback template pairs are as follows:

$$A_{m,n}^{(1)} = \begin{cases} \dfrac{l_t(m,n)}{l_t(i,j)} & \text{if } h(I) \times s_t(m,n) \ge s_t(i,j) \\ 0 & \text{else} \end{cases} \quad (6)$$

$$A_{m,n}^{(2)} = \begin{cases} \dfrac{h(I) \times s_t(m,n)}{s_t(i,j)} & \text{if } h(I) \times s_t(m,n) \ge s_t(i,j) \\ 0 & \text{else} \end{cases} \quad (7)$$

here I is the image intensity vector (for a colored image it would have 3 components) and $h(I)$ is a monotonous decreasing intensity difference function. When $g(.)$ is selected such that $y_t(i, j) = x_{t-1}(i, j)$, the input and b are set to 0, and r is set to 1, this modified design would allow interactive, multi-label segmentation of images for which conventional segmentation algorithms may fail. To do this, the user initiates segmentation by interactively selecting the voxels on the image for a number of labels aimed. The initial label of each selected voxel is set to a unique number greater than 1 while the strength of each selected voxel is set to 1 (the maximum possible value). The initial strengths and the initial labels of the remaining voxels (left unselected) are all set to 0. After each iteration of the multi-state CNN algorithm, the strength values change towards 1, except those selected by the user. As the process stabilizes, this change will eventually go towards zero. Therefore the iteration is stopped when the total change does not vary from iteration to iteration. Vezhnevets et al reports such a design dedicated to process only 24-bit images with RGB color space [18]. When grayscale depth and high spatial resolution nature of the MR images are considered, the design requires some modifications and if done, it would also require intensive user guidance and long computation times for any numerical implementation.

To improve the design for use in medical image processing, first, we propose the use of the following difference function that works with normalized intensity values:

$$h(\tilde{I}) = \exp^{-\frac{1}{2\sigma^2} \times \left(\tilde{I}(i,j) - \tilde{I}(m,n)\right)^2} \quad (8)$$

where σ is the standard deviation, $\tilde{I}$ is the intensity normalized image computed from the image I using

$$\tilde{I} = \frac{I - \min(I)}{\max(I) - \min(I)} \qquad (9)$$

where $\min(\cdot)$ and $\max(\cdot)$ denote the minimum and maximum operators.

Second, we propose the use of multi-level multi-resolution pyramid reduction for the images to be processed and the use of multi-state CNNs connected in cascade to minimize user guidance and to shorten numerical computation time (see Fig. 1). The original (acquired) image is first resized using the 2-level Gaussian pyramid reduction defined in [19]. From the second level pyramid of the image, the voxels for 3 classes namely background, breast and chest are selected by the user. These 'labeled' voxels and the second level pyramid of the original image are the inputs of the first multi-state CNN, $mCNN_1$. The output of $mCNN_1$ is eroded using a circle shaped kernel with a radius of 6 voxels determined empirically and then expanded using Gaussian pyramid interpolation described in [19]. The resultant image and the first level pyramid of the image are feed to the inputs of the second CNN, $mCNN_2$. The output of $mCNN_2$ is eroded using the same kernel employed in the previous level and then expanded. The resultant image and the acquired image are the inputs of the third CNN, $mCNN_3$. The output of $mCNN_3$ gives the segmented breast. The method described above is numerically implemented using Matlab R2010a (The MathWorks Inc., USA).
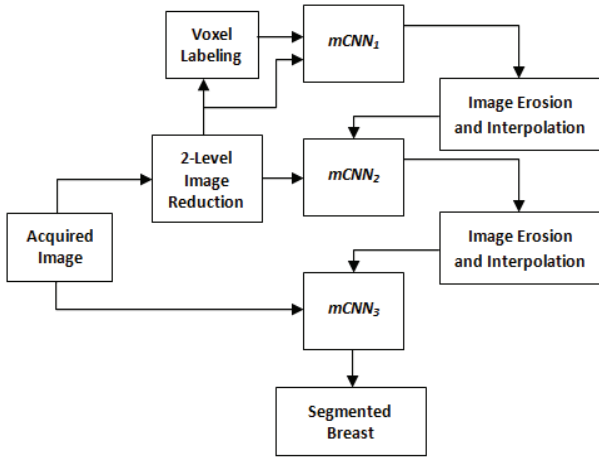

Fig.1. Simplified flowchart of the developed segmentation algorithm

2.4. Performance Evaluation

Success of the proposed segmentation algorithm is quantified with several metrics computed from the region estimated automatically by this method and the region delineated manually by an expert. In this study, to minimize the time required for manual segmentations, manual corrections to computerized segmentations are used. Let C_s be the set of voxels within the breast region estimated by our segmentation method, C_r be the set of voxels delineated manually and $n_\Re$ be the total number of voxels within region $\Re$. Segmentation precision PR is calculated using [20]

$$PR(C_s, C_r) \ (\%) = \frac{n_{C_s \cap C_r}}{n_{C_s \cup C_r}} \times 100 \qquad (10)$$

Segmentation accuracy is assessed using the true-positive volume fraction $TPVF$ and false-positive volume fraction $FPVF$ percentages calculated by [20]

$$TPVF(C_s, C_r) \ (\%) = \frac{n_{C_s \cap C_r}}{n_{C_r}} \times 100 \qquad (11)$$

$$FPVF(C_s, C_r) \ (\%) = \frac{n_{C_s - (C_s \cap C_r)}}{n_{C_r}} \times 100 \qquad (12)$$

$TPVF$ is the fraction of total amount of voxels delineated by the expert that was covered by our method and $FPVF$ is the voxels falsely identified by our method as a fraction of the amount of the voxels delineated by the expert. Clearly, the greater the PR and the $TPVF$ and the smaller the $FPVF$ values are, the better will be the segmentation.

3. Results

106 non-fat suppressed T2-weighted high resolution breast MR images from twenty-three women that covered 36 fatty, 42 fibrogulandular or heterogeneously dense and 28 dense breast slices in a range of sizes were analyzed using the developed algorithm. Plots for the cumulative percentage of segmented breasts versus calculated segmentation performance metrics are presented in Figs. 2a-2c. From these curves, it can be observed that the performance of the algorithm is quite satisfactory. On the average, at a PR threshold of 94%, some 95% of the breasts are segmented precisely. At a $TPVF$ threshold of 94%, 99% of the breasts are segmented correctly and only 9.4% of the breasts are misclassified at a $FPVF$ threshold of 0.2%. The segmentation algorithm performs well with high precision, high true-positive volume fraction and very low false-positive volume fraction with a performance of 99.1±2.0%, 99.4±1.4%, and 0.1±0.2%, respectively.
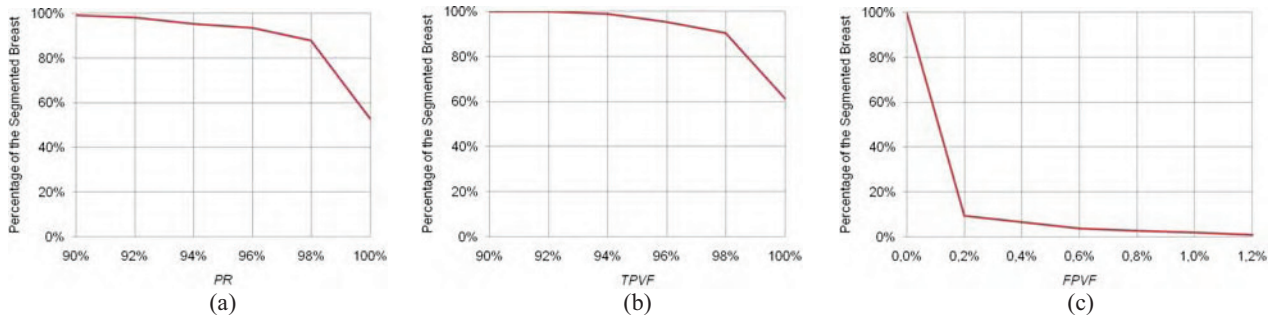

Fig. 2. Plot of cumulative percentage of the segmented breast versus (a) PR, (b) $TPVF$ and (c) $FPVF$

The efficacy of the segmentation algorithm developed here is illustrated using three cases. The first case is for a woman with a large fatty breast. Figs. 3a-3c shows the acquired image slice and computed first and second level reduced images. On the acquired image, near the right breast axilla, a high intensity inhomogeneity artifact is noticeable. User labeled voxels for background (blue solid area), breast (red solid area) and chest (green solid area) regions are seen in Fig. 3d. Figs. 3e-3f shows the automatically determined regions by applying morphological image erosion followed by image expansion to the outputs of $mCNN_1$ and $mCNN_2$, respectively. Boundary of the segmented breast (the output of $mCNN_3$) is seen in Fig. 3g. Segmentation performance for this case is very good although there is a high intensity inhomogeneity artifact near the right breast axilla (PR=99.7%, $TPVF$=99.8% and $FPVF$=0.04%). False-positives are due to a blood vessel located near to the skin of the left breast.

(a)

(b)   (c)

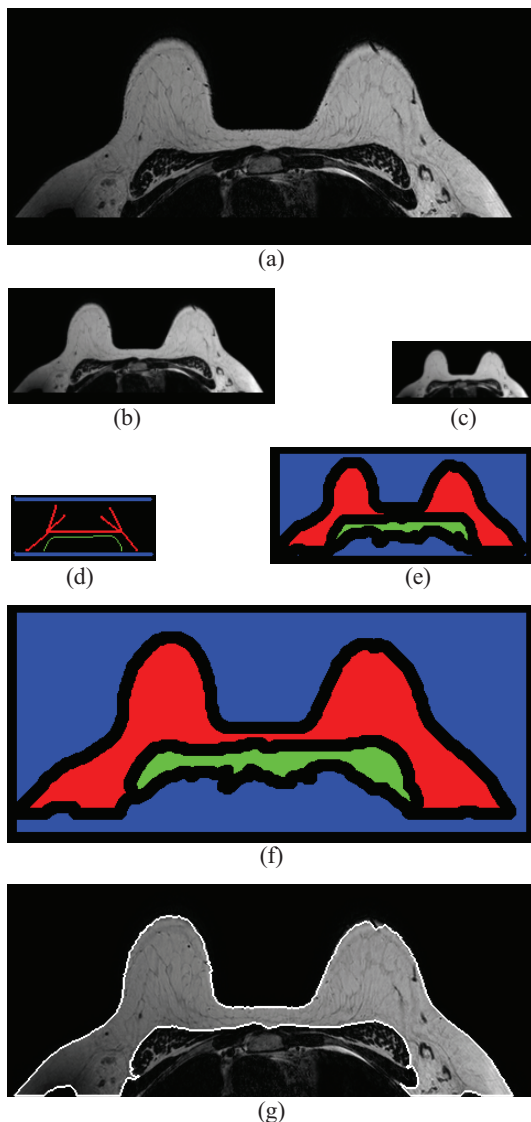(d)   (e)

(f)

(g)

Fig. 3. Fatty breast. (a) Acquired image and (b, c) computed 1st and 2nd level reduced images, (d) labeled voxels, (e, f) eroded and expanded outputs of $mCNN_1$ and $mCNN_2$ (g) Segmented breast boundary superimposed onto the acquired image

Acquired image of a medium and heterogeneously dense breast with fatty tissue connected to the chest wall is shown in Fig. 4a. The image is noisy and corrupted by partial volume artifacts. Computed first and second level reduced images are given in Figs. 4b and 4c. User labeled voxels for background, breast and chest regions are seen in Fig. 4d. Figs. 4e and 4f show the results of image erosion and expansion applied to the outputs of $mCNN_1$ and $mCNN_2$, respectively. Boundary of the segmented breast is seen in Fig. 4g. Segmentation performance for this case is excellent (PR=100%, $TPVF$=100% and $FPVF$=0.00%).

(a)

(b)   (c)

(d)   (e)
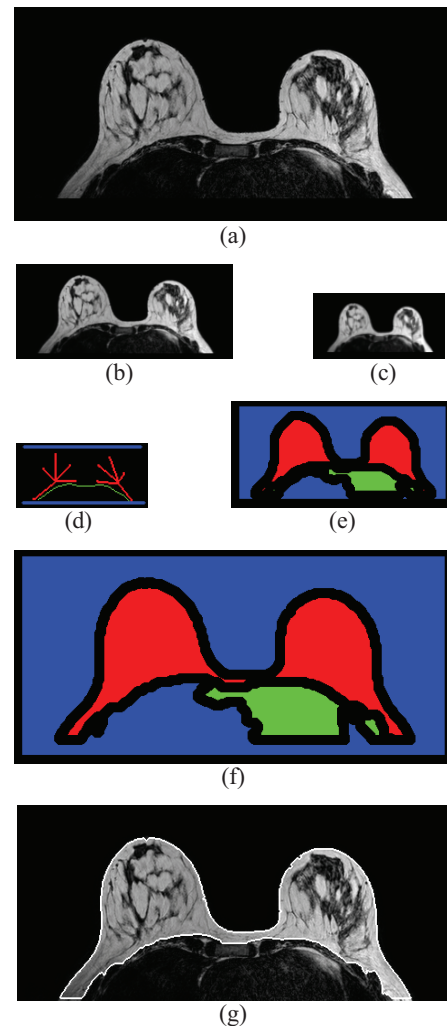

(f)

(g)

Fig. 4. Heterogeneously dense breast. (a) Acquired image, (b, c) 1st and 2nd level reduced images, (d) labeled voxels, (e, f) eroded and expanded outputs of $mCNN_1$ and $mCNN_2$, (g) segmented breast boundary

In the third case, a woman with a medium and dense breast is considered. As seen in Fig 5a, fibroglandular tissue is connected to the chest wall and some fatty tissue is present right underneath the midsternum. User selected voxels and automatically labeled voxels in the next steps are seen in Figs. 5b, 5d and 5f. Boundary of the segmented breast is seen in Fig. 5g. Segmentation performance for this case is good (PR= 98.3%, $TPVF$=100% and $FPVF$= 0.38%). False-positives are all due to chest wall muscles.
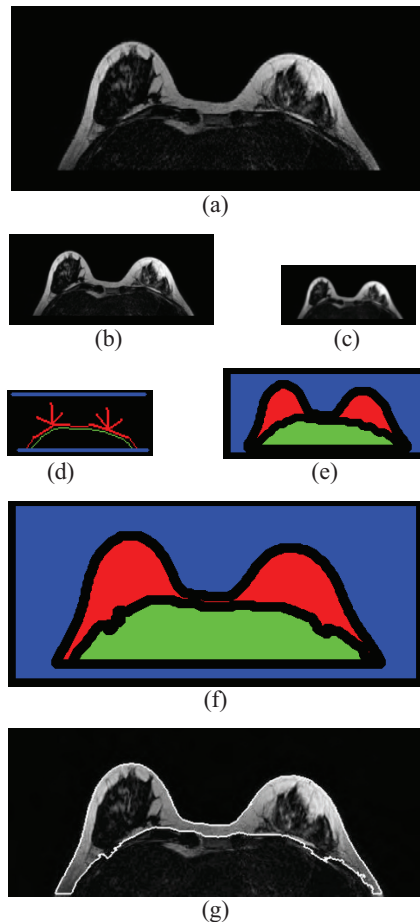
(a)

(b)   (c)

(d)   (e)

(f)

(g)

Fig. 5. Dense breast. (a) Acquired image, (b, c) 1st and 2nd level reduced images, (d) labeled voxels, (e, f) eroded and expanded outputs of $mCNN_1$ and $mCNN_2$, (g) segmented breast boundary

4. Conclusion

For breast density assessment or lesion localization, computer assisted evaluation of MR images requires accurate segmentation of breast tissues from other tissues and regions of the body, such as the chest muscle, lungs, heart and ribs. Reported breast segmentation methods are able to generate satisfactory results for certain patients and for certain degrees of background noise, intensity inhomogeneity and partial volume artifacts. In this study, we introduce a semi-automated segmentation algorithm that uses three specially designed multi-state cellular neural networks (CNNs) connected in cascade. Statistical analysis results show that the algorithm requires minimal user interaction and exceptionally effective for segmenting the breast region. The use of multi-state CNNs reduces the false segmentations on the images due to the artifacts caused by noise, intensity inhomogeneity and partial volume. We hope that this algorithm will facilitate computer aided breast examinations for density assessment and lesion localization.

6. References

[1] C. K. Kuhl, "The current status of breast MR imaging Part I. Choice of technique, image interpretation, diagnostic accuracy, and transfer to clinical practice", *Radiology*, vol. 244, pp. 356-78, 2007.

[2] C. K. Kuhl, S. Schrading, H. B. Bieling, E. Wardelmann, C. C. Leutner, R. Koenig et al., "MRI for diagnosis of pure ductal carcinoma in situ: a prospective observational study", *The Lancet*, vol. 370, pp. 485-92, 2007.

[3] M. Khazen, R.M.L. Warren, C.R.M. Boggis, E.C. Bryant, S. Reed, et al., "A pilot study of compositional analysis of the breast and estimation of breast mammographic density using three-dimensional T1-weighted magnetic resonance imaging", *Cancer Epidemiol Biomarkers Prev*, vol. 17, pp. 2268-74, 2008.

[4] S. Behrens, H. Laue, M. Althaus, T. Boehler, B. Kuemmerlen, et al., "Computer assistance for MR based diagnosis of breast cancer: Present and future challenges", *Comput Med Imag Graph*, vol. 31, pp. 236-47, 2007.

[5] P. Hayton, M. Brady, L. Tarassenko, N. Moore, "Analysis of dynamic MR breast images using a model of contrast enhancement", *Med Imag Anal*, vol. 1, pp. 207-24, 1997.

[6] M. Koenig, S. Kohle, H.O. Peitgen, "Automatic cropping of breast regions for registration in MR mammography", in Proc. SPIE, 2005, pp. 1563-70.

[7] W. Lu, J. Yao, C. Lu, S. Prindiville, C. Chow, "DCE-MRI segmentation and motion correction based on active contour model and forward mapping", in Proc. SNPD, 2006, pp. 208–212.

[8] K. Nie, J. Chen, S. Chan, M.I. Chau, H.J. Yu, et al., "Development of a quantitative method for analysis of breast density based on three-dimensional breast MRI," *Med Phys*, vol. 35, pp. 5253-62, 2008.

[9] L. Arbach, "Breast MRI: Segmentation and classification", Ph.D. Thesis, 2004.

[10] T. Twellmann, O. Lichte, T.W. Nattkemper, "An adaptive tissue characterization network for model-free visualization of dynamic contrast enhanced magnetic resonance image data," *IEEE Trans Med Imaging*, vol. 24, pp. 1256-66, 2005.

[11] N. Otsu, "A threshold selection methods from gray-level histograms", *IEEE Trans Syst Man Cybernet*, vol. 9, pp. 62-6, 1979.

[12] G. Ertas, H.O. Gulcur, M. Tunaci, M. Dursun, "k-means based segmentation of breast region on MR mammograms", *MAGMA*, vol. 19, supp. 1, pp. 317, 2006.

[13] J. Yao, J.A. Zujewskia, J. Orzano, S. Prindiville, C. Chow, "Classification and calculation of breast fibroglandular tissue volume on SPGR fat suppressed MRI", in Proc. SPIE, 2005, pp. 1942-9.

[14] G. Ertas, H.O. Gulcur, M. Tunaci, O. Osman, O.N. Ucan, "A preliminary study on computerized lesion localization in MR mammography using 3D nMITR maps, multilayer cellular neural networks, and fuzzy c-partitioning", *Med Phys*, vol. 35, pp. 195-205, 2008.

[15] M. H. Brugge, "Morphological Design of Discrete-Time Cellular Neural Networks", Ph.D. thesis, Groningen, 2005.

[16] H. Harrer, J. A. Nossek, and R. Stelzl, "An analog implementation of discrete-time cellular neural networks", *IEEE Trans Neural Netw*, vol. 3, pp. 466–476, 1992.

[17] K. R. Crounse and L. O. Chua, "Methods for image processing and pattern formation in cellular neural networks: a tutorial", *IEEE Trans Circuits Syst*, vol. 42, pp. 583–601, 1995.

[18] V. Vezhnevets, V. Konouchine, "GrowCut - Interactive multil-label N-D image segmentation by cellular Automata", in Proc. GraphiCon, 2005.

[19] P.J. Burt and E.H. Adelson, "The laplacian pyramid as a compact image code", *IEEE Trans on Commun*, vol. COM-31, pp. 532-540, 1983.

[20] J. K. Udupa, V. E. LeBlanc, Y. Zhuge, C. Imielinska, H. Schmidt, L. Currie, B. E. Hirsch, and J. Woodburn, "A framework for evaluating image segmentation algorithms", *Comput Med Imaging Graph*, vol. 30, pp. 75–87, 2006.